Simulations of film stress effects on mirror segments for the Lynx X-ray Observatory concept

Brandon D. Chalifoux
Youwei Yao
Ralf K. Heilmann
Mark L. Schattenburg

Simulations of film stress effects on mirror segments for the Lynx X-ray Observatory concept

Brandon D. Chalifoux,[a,b] **Youwei Yao,**[b] **Ralf K. Heilmann,**[b] **and Mark L. Schattenburg**[b,*]
[a]Massachusetts Institute of Technology, Department of Mechanical Engineering, Cambridge, Massachusetts, United States
[b]Massachusetts Institute of Technology, Kavli Institute for Astrophysics and Space Research, Cambridge, Massachusetts, United States

Abstract. The Lynx X-ray Observatory concept, under study for the 2020 NASA Decadal Survey, will require a telescope with ∼2 m² of effective area and a point-spread function (PSF) with ∼0.5-arc sec half-power diameter (HPD) to meet its science goals. This requires extremely accurate thin grazing-incidence mirrors with a reflective x-ray coating. A mirror coating, such as 15-nm-thick iridium, can exhibit stress exceeding 1 GPa, significantly deforming segmented mirrors and blurring the PSF. The film stress and thickness are neither perfectly repeatable nor uniform. We use finite element analysis and ray tracing to quantify the effects of integrated stress inaccuracy, nonrepeatability, nonuniformity, and postmounting stress changes on segmented mirrors. We find that if Lynx uses segmented mirrors, it will likely require extremely small film stress (∼10 MPa) and nonuniformity (<1%). We show that realigning mirrors and matching complementary mirror pairs can reduce the HPD from uniform film stress by a factor of 2.3× and 5×, respectively. Doubling mirror thickness produces much less than the 4× HPD reduction that would be expected from a flat mirror. The x-ray astronomy community has developed numerous methods of reducing the PSF blurring from film stress, and Lynx may require several of these in combination to achieve 0.5 arc sec HPD using segmented mirrors. © *The Authors. Published by SPIE under a Creative Commons Attribution 4.0 Unported License. Distribution or reproduction of this work in whole or in part requires full attribution of the original publication, including its DOI.* [DOI: 10.1117/1.JATIS.5.2.021004]

Keywords: Lynx; x-ray; film stress; simulation; stress compensation.

Paper 18096SS received Nov. 1, 2018; accepted for publication Feb. 13, 2019; published online Mar. 9, 2019.

1 Introduction

The Lynx X-ray Observatory mission concept (or Lynx) is under study for the 2020 NASA Astrophysics Decadal Survey and is expected to enable significant progress in astrophysics and cosmology.[1] In order to achieve its scientific goals, Lynx will require a telescope with a ∼2 m² effective area for 1 keV x-rays, and an on-axis point-spread function (PSF) with ∼0.5 arc sec half-power diameter (HPD). Lynx requires the use of thin grazing-incidence mirrors, around 0.5 mm thick for segmented mirror designs[2,3] or around 2 mm for full-shell mirror designs,[4] to achieve the effective area requirements while satisfying mass and diameter limitations of current launch vehicles. This paper is restricted to the investigation of film stress effects on the shape of segmented silicon mirrors. To produce an x-ray mirror segment, a silicon substrate must be fabricated[5] and then coated, typically with a thin metal film, such as iridium[6–9] or a multilayered coating,[10–12] to efficiently reflect x-rays. Coatings are often deposited using magnetron sputtering, usually to maximize x-ray reflectivity, which results in a stressed film that deforms the thin mirror substrates, especially segmented mirrors. This problem is well known to the community; the Lynx Interim Report[13] cites mitigating the effects of coating stress as one of the major technology development goals.

Film stress is one of many effects that can cause PSF blurring. It is reasonable to expect that the error allocation to coating stress for Lynx will be in the (wide) range of 0.05 to 0.20 arc sec HPD. In the sections that follow, we adjust film stress such that its total HPD contribution for each studied effect falls within this range. In all of the simulations presented in this paper, the HPD is proportional to the integrated stress up to at least twice as high as we present, so adjusting these results to a particular error allocation is simple.

The importance of minimizing the integrated film stress N_f, defined as the film stress integrated through the coating thickness, on thin segmented mirrors has been known for over two decades.[14] Many authors (e.g., Cohen and Foster[15] and Parodi[16]) within the x-ray telescope mirror community have performed studies evaluating the effects of film stress using finite element (FE) analysis and ray tracing. Cohen and Foster[15] presented one such study of full shell mirrors and conical mirror segments deformed by uniform film stress, for a variety of mirror geometry parameters. Their study showed that even very small integrated stress ($N_f = 0.5$ N/m, or 33 MPa for a 15 nm film) can deform segmented glass mirrors of many geometries to produce a PSF much larger than 0.1 to 0.2 arc sec HPD. In this paper, we also use FE analysis and ray tracing, as detailed in Sec. 2. In addition, we implement a faster linearized ray tracing method (showing that it agrees with ray tracing), and we consider diffraction effects. This study is limited to silicon mirror segments with a fixed mirror length and arc-width, as described in Sec. 2.

An ideal x-ray coating would have maximum reflectivity (for a single-layer film, this requires high film density and low roughness) and no stress. However, in addition to suboptimal reflectivity, real coatings will have integrated stress inaccuracy (nonzero but uniform integrated stress), nonrepeatability (uniform integrated stress that varies from mirror to mirror), nonuniformity (integrated stress that varies with position on the mirror), and postmounting changes (integrated stress that varies with time or temperature, after mounting). We present simulation results for the PSF blurring that occurs because of these four

*Address all correspondence to Mark L. Schattenburg, E-mail: marks@space.mit.edu

types of errors, for segmented silicon mirrors of 100 mm length, around 100 mm width, 0.5 mm thickness, and radii between 250 and 1500 mm. We also analyze several methods that can reduce PSF degradation from these types of errors. We consider these four types of errors in isolation, but we recognize that there may be important interactions between them. There is no published analysis of the last three of these errors, and no published analysis of the potential mitigation strategies for accuracy and repeatability errors.

Several technologies intended to address the film stress problem are under development, and each addresses one or more of the types of errors described above. One approach is to use deposition conditions that result in minimum integrated film stress while not significantly degrading x-ray reflectivity.[6,11,17,18] Depositing the same film (or a different film with the same integrated stress) on both sides of the mirror[8,9,19] enables a wider range of deposition conditions to optimize reflectivity and can also result in a thermally balanced mirror. The ability of either of these methods to solve the film stress problem may be limited by uniformity of the integrated stress, since thickness uniformity alone is typically around ±1%,[9] and stress may also vary over the mirror surface. We will discuss this issue in more detail in Sec. 4. Annealing can reduce, but may be incapable of eliminating, the iridium film stress, and also results in some nonuniformity.[8]

Several approaches are under development to provide nonuniform integrated stress compensation (NISC), such as silicon oxide patterning,[20,21] ion implantation,[22] active mirrors,[3] differential deposition,[23,24] substrate biasing during deposition,[25] magneto-strictive films,[26] and laser microstressing.[27] As of this writing, silicon oxide patterning has been the only method applied to x-ray mirror segments to compensate for nonuniform film stress.[20] Further improvement is necessary for large-radius mirrors. Moreover, it is likely necessary to combine one of the methods from above with one of the NISC methods.

2 Methodology

We use a combination of FE analysis and ray tracing to simulate four types of errors: stress inaccuracy, nonrepeatability, nonuniformity, and changes after mounting. In Sec. 2.1, we detail the ray tracing procedure, and in Sec. 2.2 we describe a linearized ray tracing method that is significantly faster than ray tracing, and accurate for the small mirror deformations that we consider in this paper. We also compare this method to the one-dimensional Fresnel diffraction calculation described by Raimondi and Spiga.[28] In Sec. 2.3, we describe the FE models in detail and describe how the results of this paper may (or may not) be accurately scaled.

The mirrors for x-ray telescopes are usually nested shells of grazing-incidence mirrors, where each shell has a primary mirror surface and a secondary mirror surface. The shells can be monolithic or split into segments, as we consider in this paper. The telescope and mirror segment geometry used throughout this paper is shown in Fig. 1. Lynx is expected to have a mirror assembly that is about 3 m in diameter,[1] so we study segments from six shells with radii ranging from 250 to 1500 mm, where the shell radius (R) is defined at the intersection of the primary and secondary mirrors (P-S intersection). The primary and secondary mirrors have no gap between them. We fix the primary mirror length (L_p) at 100 mm and we choose the mirror angular width (W) such that the arc-width at the P-S intersection is at least 100 mm and an even number of segments
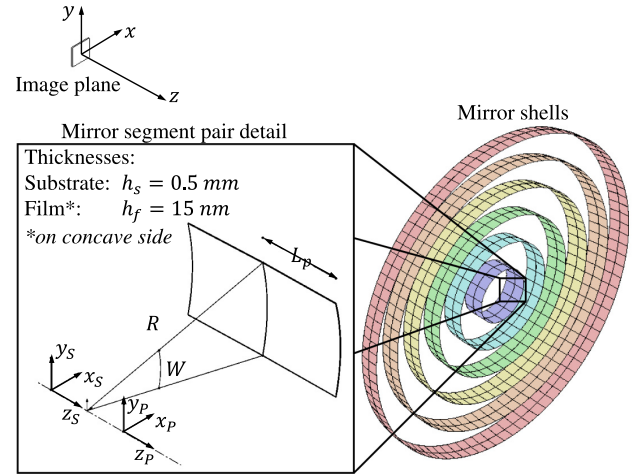

Fig. 1 Diagram of telescope and mirror pair geometry.

fit into a shell (with no gaps). The focal length (f) is fixed in all cases to 10 m. Each silicon mirror substrate has the same thickness (h_s) of 0.5 mm, and the iridium film thickness (h_f) is 15 nm. Mirror segments have an integrated film stress (N_f) applied to the concave surface. The mirror segments have two independent coordinates: axial (z) and azimuthal (θ) position.

The optical prescription, such as the Wolter Type I[29] or Wolter-Schwarzschild[30] design, affects imaging aberrations, but they both produce perfect on-axis images, and both prescriptions are nearly conical. We specify the optical prescription to be that of a Wolter I design, although in the FE models we use the corresponding conical approximation. We choose the grazing angles (α) on the primary and secondary mirrors to be the same, and L_p and f have been fixed, leaving R to define the optical system. The length of the secondary mirror (L_s) is calculated as in VanSpeybroeck and Chase,[29] and is nearly the same as the length of the primary mirror.

2.1 Ray Tracing

We use Monte Carlo ray tracing for the analysis in Sec. 3.1. For a primary and secondary mirror segment pair, we first calculate the surface coordinates and normal vectors for each mirror, at a regular grid of azimuth and axial coordinates, all defined in the global coordinate frame shown in Fig. 1. The coordinates and normal vectors include any deformation (calculated from the FE model) as well as rigid-body rotations and translations. We then randomly select 2000 azimuth and axial coordinates on the primary mirror segment and calculate the reflection of on-axis rays off the primary mirror surface. We determine the intersection of these rays with the secondary mirror surface and calculate the reflected ray trajectories. Finally, we calculate the intersection of these rays with the image plane. Since each mirror pair has the same deformation, we copy and rotate these rays for each of the other mirrors within the same shell. The intersection points on the image plane form a spot diagram.

From the spot diagram, we calculate the HPD, defined as twice the angular radius at which the encircled energy function (EEF) is 0.50, for a single shell. Since each ray from a single shell represents roughly the same effective area, the HPD for a shell in isolation is twice the median angular ray radius

$$\text{HPD}_{\text{shell}} = 2 \times \text{median}\{\phi_i\}, \qquad (1)$$

where $\phi_i = (x_i^2 + y_i^2)^{1/2}/f$ is the angular radius for ray i, and x_i and y_i are the ray coordinates on the image plane.

We also estimate the HPD for all shells by weighting each ray by the relative effective area it represents (this HPD estimate is meant as a general guide, but it ignores any diffraction effects, which can be significant for mirrors with small radii, as shown in Sec. 2.2). Lynx would have many more than six shells, and we assume each of the six shells we analyze (each designated by index j) is representative of all closest shells in an actual telescope design. We account for blockage from the mirror thickness, and reflectivity[31] (ρ) of 1 keV x-rays at grazing angle α_j from a 15 nm iridium film with 0.4 nm root mean-squared (RMS) roughness. Based on these considerations, the effective area (A_j) represented by shell j is

$$A_j = \frac{L_p \sin \alpha_j}{L_p \sin \alpha_j + h_s} \rho^2 \pi (R_{j,\text{upper}}^2 - R_{j,\text{lower}}^2), \qquad (2)$$

where $R_{j,\text{upper}} = (R_j + R_{j+1})/2$ and $R_{j,\text{lower}} = (R_{j-1} + R_j)/2$ (for the largest radius, R_6, we take $R_7 = R_6$, and for the smallest radius, R_1, we take $R_0 = R_1$). The factor ρ^2 is present due to two reflections. The relative weight of rays from each shell, $\eta_j = A_j/\Sigma_j A_j$, is listed in Table 1. The EEF can be calculated from the weight of each ray i as

$$\text{EEF}(\phi) = \sum_i \eta_i (\phi_i \leq \phi) / \sum_i \eta_i. \qquad (3)$$

To verify the accuracy of the ray tracing code, we replicated the ray tracing results of VanSpeybroeck and Chase[29] for off-axis rays and perfect mirrors and found good agreement. We also replicated the 27 cases studied by Cohen and Foster[15] and found <1% difference in the RMS diameter (RMSD). We also show, in Fig. 2, that this ray tracing agrees with the linearized ray tracing method described in Sec. 2.2.

2.2 Linearized Ray Trace Approximation Method

Our goal is to calculate the EEF for a given mirror deformation data, such as from an FE model. A simplified approximation approach to ray tracing can be used in situations where the mirror deformation is small and the illumination is on-axis. We will refer to this as the linearized ray trace method. For a perfect Wolter I mirror pair, rays that reflect off the front (entrance side

Table 1 Reflectivity and weight for rays reflecting off each shell, for 1 keV x-rays with a film and substrate roughness of 0.4 nm RMS. The weight for a shell j is $\eta_j = A_j/\Sigma_j A_j$, and the effective area A_j is calculated using Eq. (2).

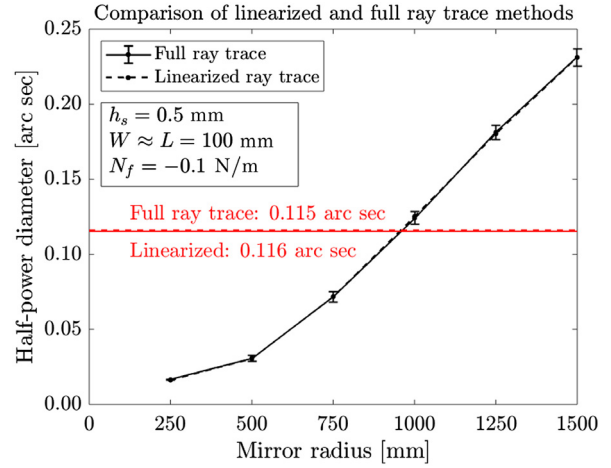| Shell radius (mm)	Reflectivity, ρ	Weight, η
250	0.931	0.040
500	0.865	0.140
750	0.802	0.200
1000	0.739	0.238
1250	0.676	0.258
1500	0.612	0.124

Fig. 2 Comparison between linearized and full ray trace methods, for a uniform integrated stress of $N_f = -0.1$ N/m (compressive). The full ray trace HPD is evaluated at the nominal focus. For small deformations, there is minimal difference between the two methods. The error bars represent the standard deviation of HPD from 10 repetitions of the full ray trace, which used 2000 rays per mirror. The red horizontal lines represent the HPD for all shells together, calculated using Eq. (3).

along the optical axis) of the primary mirror subsequently reflect off the back (exit side along the optical axis) of the secondary mirror, and rays that reflect off the back of the primary mirror subsequently reflect off the front of secondary mirror. For a mirror with small radial deformation and small slope errors, a ray that reflects off the primary mirror will intersect the secondary mirror very close to the nominal intersection point, an assumption that we discuss below. In addition, since the rays are near grazing incidence to the mirrors, the axial slope has a significantly larger effect than the azimuthal slope. The angular ray deviation ϕ_i after reflecting off the secondary mirror, relative to the perfect mirror case, is then,

$$\phi_i \approx 2[-\beta_P(\theta_i, z_i) + \beta_S(\theta_i, z_i)], \qquad (4)$$

where $\beta_P(\theta_i, z_i)$ and $\beta_S(\theta_i, z_i)$ are axial slope errors of the primary and secondary mirrors, respectively, at a pair of nominal intersection points. The HPD for an isolated shell is calculated using Eq. (1), and for the full telescope using Eq. (3). Figure 2 shows that the agreement between this method and full ray tracing is well within the random variations of the ray tracing. We found similar agreement even for integrated stress values 20× larger (we did not test stresses larger than this).

We make two assumptions: (i) the ray deviation due to azimuthal slope is small compared to the deviation due to axial slope, and (ii) the actual and nominal ray intersection points on the secondary mirror are identical. Assumption (i) results in an error in the ray deflection angle roughly equal to $\frac{1}{2}(\frac{\gamma}{\beta})^2 \sin^2 \alpha$, where β and γ are the axial and azimuthal slope errors, respectively. This error is typically much less than 1%. Assumption (ii) can also lead to errors because the actual ray intersection point has a larger or smaller radius and a different nominal slope. If the slope error is small compared to the nominal mirror axial slope, then for a Wolter I prescription this error is roughly equal to $3.5 \times L_p/f$, or around 3.5% for a 10 m focal length and 100 mm long mirrors. Radial height errors also affect the PSF, but for the values of film stress here, the effect is small. For

example, a 20 nm height error (see Fig. 4) results in a displacement at the focal plane equivalent to only 0.0004 arc sec.

This method should not be used when mirrors have large alignment changes (as in Sec. 3) since the linear and angular errors can be significant. Full ray tracing also enables one to evaluate effects of misalignment on effective area, which this linearized method ignores. However, for mirrors that only have a small integrated film stress (uniform or non-uniform), the slope errors are small and this method provides a very fast means of calculating the HPD.

In some cases, diffraction may have an important effect on the PSF. Certainly, for the smallest radii and for soft x-rays (~1 keV), diffraction from the mirror annulus (aperture diffraction) can be significant, as shown in Fig. 3. More relevant to understanding the effects of film stress, however, is the fact that for a PSF with 0.5 arc sec HPD, even low spatial frequency errors scatter light out of the core of the PSF for small grazing angles and soft x-rays. Ray tracing may under- or overestimate the HPD resulting from film stress. We have calculated the HPD using the two-mirror 1-D Fresnel diffraction calculation from Ref. 28, for 1 keV x-rays reflecting off undeformed mirrors (where the HPD is entirely a result of aperture diffraction) and deformed mirrors (where the HPD is affected by both aperture diffraction and the deformation). We do not consider any effects of roughness on the PSF. We use the minimum sampling period from Ref. 28 for the primary mirror, and we use half the minimum sampling period for the secondary mirror and the detector (whose angular extent is ± 0.5 arc sec). We calculate the PSF of a mirror pair by averaging the PSF from 16 axial lines.

Figure 3 shows the HPD resulting from this diffraction calculation alongside the HPD resulting from the linearized ray trace method. For the three largest radii, the HPD calculated using Fresnel diffraction agrees with that of the linearized ray trace, confirming that in this case, the linearized ray tracing result is accurate. For the smallest three radii, aperture diffraction dominates the PSF, causing the two calculation methods to diverge. Since we are interested in the contribution from film
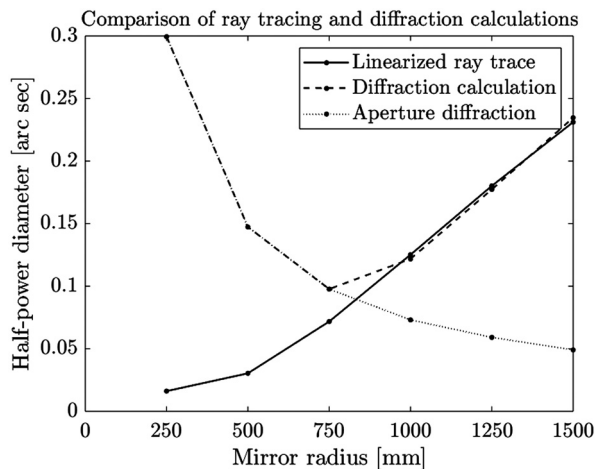
stress alone, and we did not separate the effect of film stress from that of aperture diffraction, we do not know exactly how well the linearized ray trace calculation agrees with that of the diffraction calculation for the three smallest radii.

2.3 Finite Element Analysis

We calculate the deformation of the mirror using an FE model built in ADINA, a commercial FE analysis software. The model for a mirror segment consists of one conical shell for the substrate and a second conical shell for the coating. The largest and smallest radii of the substrate shell match those of either the primary or secondary mirror geometry. The second shell is radially displaced by half of the substrate thickness and is bonded to the substrate. The substrate is 0.5 mm thick and is composed of silicon, with elastic modulus 169 GPa and Poisson's ratio 0.069 (the elastic constants for a (100) wafer crystal orientation[32]). At the end of this section, we will justify treating silicon, an orthotropic material, as an isotropic material. The coating is 15 nm thick iridium, with elastic modulus 528 GPa and Poisson's ratio 0.26.[33] At the end of this section, we will show that the mirror deformation is not sensitive to the values of the elastic constants of a thin film.

Both shells (substrate and film) have uniform rectangular meshes, with 60 elements in the axial direction and 40 elements in the azimuthal direction. Each element is a nine-node shell element, which has quadratic displacement interpolation functions (shell elements assume a linear displacement variation through the shell thickness, which is accurate for small deformations and thin shells). Since the deformation considered in this paper is at least four orders of magnitude smaller than the substrate thickness, we may assume small deformations in the FE model. The film stress is applied by prescribing a temperature field (which may be nonuniform) to the coating shell. A similar model was used by Chalifoux[34] for flat and curved substrates. For a flat plate, the model agreed with an analytical model to within 0.25% for nonuniform integrated stress fields, and much better for uniform stress. For this model, the calculated deformation of curved substrates approached that of a flat plate as the radius increases.

In Secs. 3 and 4, we are interested in analyzing mirrors that have not yet been mounted, so the FE model is kinematically constrained, and rigid body motions are removed from the calculated deformation. Figure 4 shows a typical example of the radial displacement and axial slope errors that result from a small integrated film stress.

In Sec. 5, we analyze the effect of temperature change or film stress relaxation on the mirrors after they are mounted, so we must constrain the mirrors to simulate this. We assume a four-post mount as described by Zhang et al.,[2,35] in which each post is intended to constrain translations but not local rotations. In the FE model, we apply constraints to four corner points of a 50 mm × 50 mm square centered on the mirror, at which we constrain all three translation degrees of freedom at each point. This is effectively assuming that the mounting points behave exactly as intended. In this case, we do not remove any rigid-body rotations from the FE model deformation.

We ran FE simulations on 20 kinematically mounted mirror pairs to test whether silicon crystal orientation, film thickness, film material, or substrate material significantly affect the deformation from a $N_f = -0.2$ N/m integrated stress. We ran half of these simulations using 250 mm radius and half using 1500 mm radius. For each simulation, we calculate the HPD using the
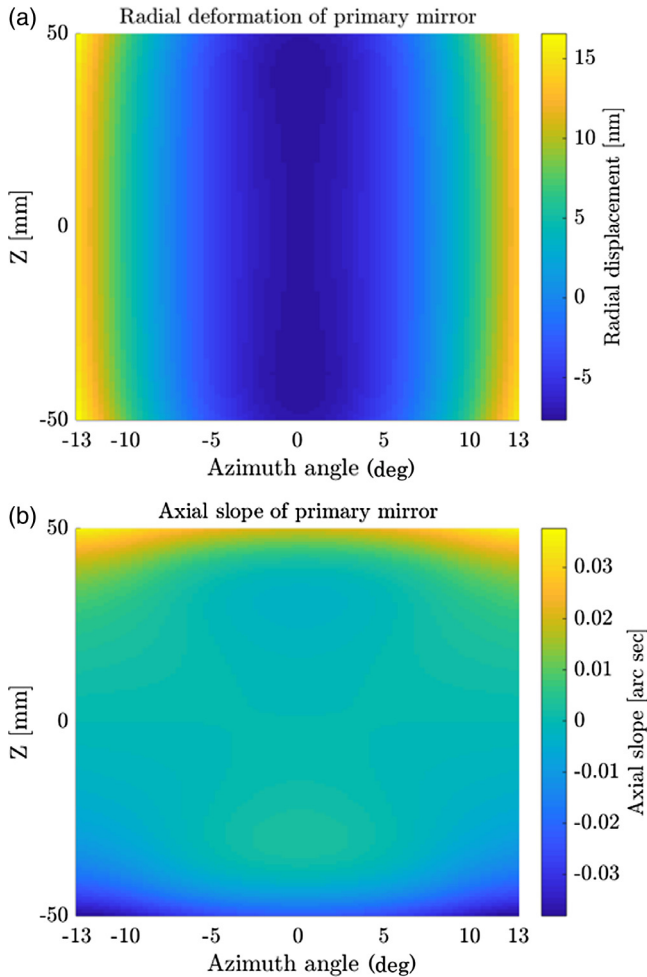

Fig. 3 Comparison of HPD calculated using linearized ray trace (solid line) and using the 1-D Fresnel diffraction calculation for 1 keV x-rays (dashed and dotted lines) described by Raimondi and Spiga.[28] The dotted line is for a perfect Wolter I mirror pair, for which the PSF is entirely due to diffraction from the mirror aperture. The dashed line includes film stress deformation ($N_f = -0.1$ N/m), and the PSFs from 16 axial lines are averaged to produce the PSF for the mirror pair.

(a)

Radial deformation of primary mirror

(b)

Axial slope of primary mirror

Fig. 4 (a) Radial deformation and (b) axial slope resulting from a uniform integrated film stress of −0.1 N/m. This is a primary mirror segment with a thickness of 0.5 mm and a radius of 250 mm. The RMS radial deformation is 6.8 nm, and the RMS axial slope is 0.0094 arc sec.

Fig. 5 RMSD as a function of substrate thickness, for various radii. RMSD decreases roughly as $h_s^{-1.25}$, which is more gradual than for a flat plate, for which deformation scales as h_s^{-2}.

linearized ray trace method described in Sec. 2.2. We also verified that the small deformation assumption is accurate by comparing the deformation results of a simulation assuming small deformations and one assuming large deformations (and 10 load steps), for integrated stress values up to 2 N/m.

We tested the effect of the silicon crystal orientation, and the effect of assuming the silicon is isotropic. We tested three orientations: the orientation at the mirror center aligned with that of a (100) wafer,[32] and this orientation rotated by 45 deg about the x- or z-axes. For the isotropic case, we used $E_s = 169$ GPa and $\nu_s = 0.069$. The relative HPD change (the range of the four cases divided by the mean of the four cases) for these experiments was 36% for $R = 250$ mm and 11% for $R = 1500$ mm, and the isotropic case is the closest to the mean. Since the effect of crystal orientation for the larger-radius mirror (which has the largest impact on the telescope HPD) is small, and since we do not know the crystal orientation of any existing mirrors, we chose to use the isotropic case for all other simulations in this paper. This also facilitates accurately scaling the results presented throughout this paper to other substrate materials.

We tested whether the HPD calculated for silicon can be scaled to other substrate materials, provided proper scaling. We found that, as for a flat plate, if the quantity $N_f(1 - \nu_s)/E_s$
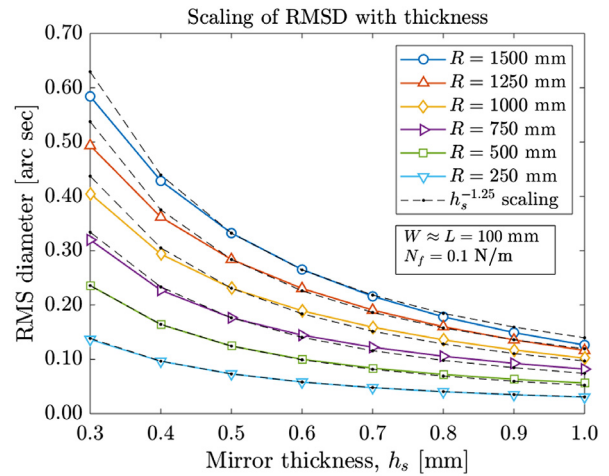
is held constant, then the HPD of a substrate made of silicon ($E_s = 169$ GPa, $\nu_s = 0.064$) or glass ($E_s = 73.6$ GPa, $\nu_s = 0.23$) are different by only 1.6% for $R = 250$ mm and 1.2% for $R = 1500$ mm.

For a thin film ($h_s/h_f > 100$), we do not expect the film thickness or material to significantly affect the deformation, provided the integrated stress is constant.[36] For a 20 nm film, the HPD calculated from two models, in which the film material is iridium or silicon, are different by 0.04% for both radii. For a 1-μm film, this difference is still only 2.3%. Since for a thin film, only the integrated stress affects deformation (not the film elastic properties or film thickness), the effect of multilayer coating integrated stress on mirror deformation is simple to extrapolate from the results presented in this paper.

Increasing the mirror thickness reduces the effect of film stress on HPD, but in a way that is dissimilar to a flat plate. For a flat plate, the stress-induced deformation (height and slope) scales as $1/h_s^2$. For the mirrors considered here, Fig. 5 shows that the RMSD scales roughly as $h_s^{-1.25}$ (the HPD also decreases as the thickness increases, as shown in Fig. 6, but it does not follow a power law). This is consistent with deformation that is determined primarily by net mid-surface forces within the substrate (as opposed to bending moments, which dominates the deformation response of a flat plate). Unfortunately, this implies that increasing thickness to reduce the effect of film stress on the HPD will have significantly less benefit than it would for a flat plate.

3 Uniform Stress Accuracy and Repeatability

Ideally, every coating would have zero integrated stress. However, even ignoring coating nonuniformity and changes in integrated stress after mounting, deposition processes will have some nonrepeatability and inaccuracy. Even if one of the NISC methods is used to reduce the effective integrated stress, there will still be some level of inaccuracy and nonrepeatability. In this section, we show the effect of these errors, and analyze the effectiveness of two methods of reducing the PSF blurring due to uniform integrated stress inaccuracy and nonrepeatability.

The effect of a very small integrated stress inaccuracy ($N_f = -0.1$ N/m ≈ 7 MPa $\times 15$ nm) is shown in Fig. 2. This integrated stress is far smaller than typically observed for iridium
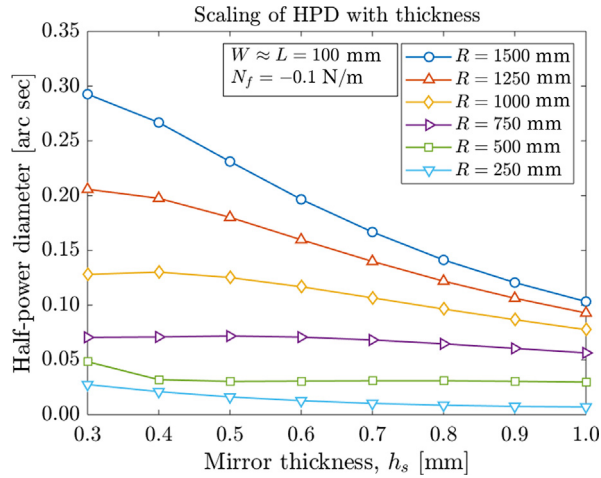
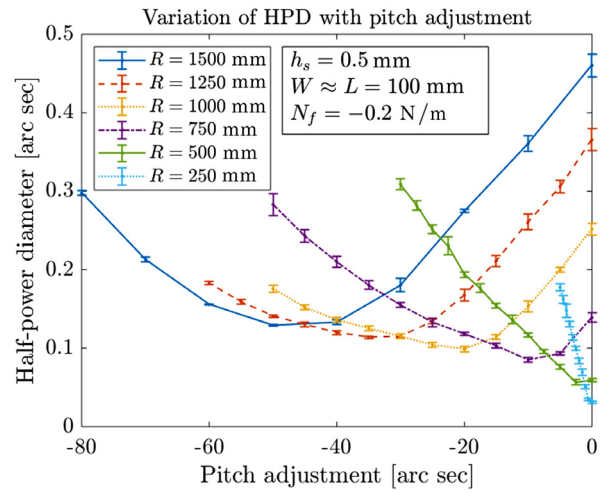**Fig. 6** HPD as a function of substrate thickness, for various radii.

Fig. 7 HPD as the pitch of primary mirrors from each shell are adjusted (and all other corresponding adjustments are made as described in the text). The error bars represent the standard deviation of five ray tracing repetitions. Negative pitch change results in a longer focal length. For each pitch change, there is a required z-translation, which varies linearly with pitch for each shell.
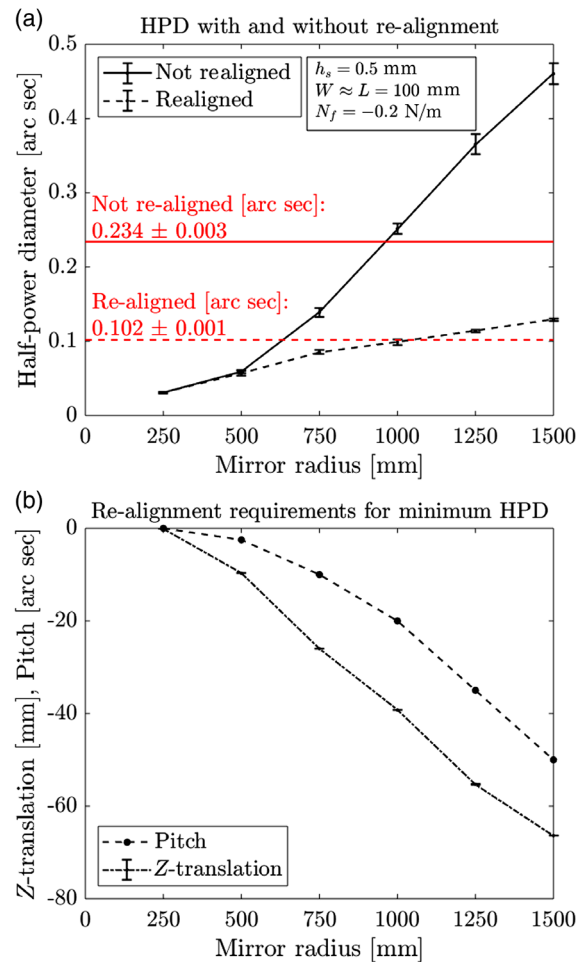
films, but it illustrates how small the stress may need to be for segmented mirrors on Lynx. Reid et al.[37] showed that various errors can be compensated by realigning the mirror segments. In Sec. 3.1, we show that a similar method can be used reduce the HPD resulting from film stress by a factor of 2.3, but it requires significant alignment changes. This method is potentially suitable for addressing integrated stress inaccuracy but not repeatability.

Another approach is to match primary and secondary mirror segments such that their slope errors tend to cancel one another. In Sec. 3.2, we analyze this approach to address integrated stress nonrepeatability, and we find that it can reduce the HPD by a factor of about 5 compared to random primary–secondary mirror pairing.

3.1 Inaccuracy Compensation Using Alignment

Since a uniform film stress causes a radial deformation that is symmetric, the only rotation that could reduce PSF blurring is the pitch (rotation about an axis centered on the mirror and parallel to the y_P- or y_S-axis, for the mirror pair shown in the inset of Fig. 1). We adjust the pitch of each primary mirror, and we adjust the secondary mirror pitch by three times this amount to maintain the same grazing angle. We also shift the mirror segments along the x_P- or x_S-axis (for the mirror pair shown in the inset of Fig. 1) to maintain alignment between their edges and avoid losing any rays. Finally, we can translate the mirrors together along either the z- or x-axis, to ensure that the rays converge near the center of the image plane. Translating the image plane along the z-axis is equivalent to translating the mirrors along the z-axis in the opposite direction, and we choose to shift the image plane rather than the mirrors. Since the rotations can be significant, we use the full ray tracing for this analysis.

Figure 7 shows the effect of changing the primary mirror pitch and z-translation (and the other associated rotations and translations described above) on the HPD from a uniform integrated stress ($N_f = -0.2$ N/m ≈ 13 MPa $\times 15$ nm). The HPD reaches a minimum because as the mirrors are translated and rotated, the contribution to HPD from misalignments increases while the contribution from the stress-induced deformation decreases. All but the two smallest mirror radii show a significant reduction in HPD, as shown in Fig. 8(a). However, the consequence of this improvement is a large required translation along the z-axis, which is shown along with the required

Fig. 8 Comparison of (a) the HPD and (b) the required z-translation and primary mirror pitch change, when the mirrors are realigned or not realigned to compensate for the film stress. The red horizontal lines represent the HPD for all shells together, calculated using Eq. (3). The error bars are the standard deviation from ray tracing.

pitch angle change in Fig. 8(b). Within a given shell, the z-translation required to minimize HPD at each pitch varies linearly with the pitch. We also tested, for $R = 1500$ mm and integrated stress of -0.1, -0.2, and -0.4 N/m, whether the minimum HPD scales linearly with integrated stress, and we found that it does. The required change in pitch and z-translation also increases approximately linearly with integrated stress.

During assembly of a meta-shell,[2,35] these alignment changes could possibly be accommodated if every mirror required the same adjustment, but adjusting each mirror (or even mirror pair) differently would likely cause assembly problems. For example, for the largest shell, if one mirror pair has $N_f = 0$ N/m and the adjacent pair has $N_f = -0.2$ N/m (which is a very small integrated stress), using this alignment approach requires these two pairs to be axially displaced from one another by nearly 70 mm. This approach is therefore potentially suitable for reducing the effect of uniform integrated stress accuracy, but probably not repeatability.

Translating the mirrors in the radial direction rather than the axial direction is also possible. For $R = 1500$ mm and $N_f = -0.2$ N/m, we found that the minimum HPD of 0.20 arc sec occurred at a pitch of -70 arc sec and a corresponding radial translation of -13.9 mm. This translation would be problematic for assembling a telescope of nested shells, so we did not pursue this approach further. Changing the axial spacing of the primary and secondary segments can also effect a focal length change, similar in magnitude to translating both mirrors along the z-axis,[37] but we did not consider this. In addition, we did not consider off-axis aberrations that may result from these alignment changes.[37]

3.2 Repeatability Compensation Using Mirror Pair Matching

Each shell of the telescope is composed of many mirror segments, which are interchangeable within a shell. Once the segments are coated and any NISC process is complete, they may each have slightly different uniform film stress values (nonrepeatability). We can sort the mirror segments to ensure that mirrors are paired such that their deformations cancel as well as possible.

In this analysis, since we need to test many mirror segments, each with a random stress value, we use the linearized ray tracing method described in Sec. 2.2, which is much faster than the full ray tracing. We assume that the number of mirrors available, from which we select pairs, is exactly the number of mirrors in the shell. Each segment is assigned a randomly distributed stress value, with a standard deviation of 1.0 N/m and a mean of 0.0 N/m. To match pairs, we sort the integrated stress on the primary mirrors in ascending order and the integrated stress on the secondary mirrors in descending order. In this way, mirrors with the most compressive (negative) integrated stress are matched with those with the most positive (tensile) integrated stress. We repeated the analysis 50 times, and the mean HPD for each radius as well as for all shells together are shown in Fig. 9. The error bars represent the standard deviation of HPD values from the 50 repetitions.

Without employing either pair matching or realignment (Sec. 3.1), the HPD is about 2.5× less sensitive to RMS nonrepeatability than to inaccuracy. The relative improvement in HPD resulting from this matching process, shown in Fig. 9, is also larger than the improvement shown in Fig. 8 for realignment. Each of these two methods addresses a different type of
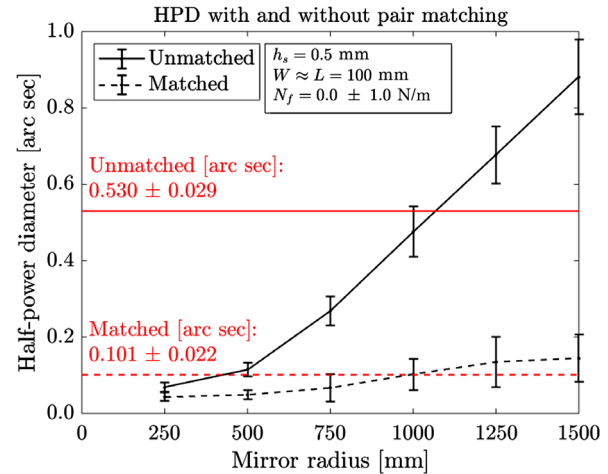

Fig. 9 Comparison of the HPD resulting from matching or not matching primary and secondary mirrors by their integrated stress. The horizontal red lines represent the HPD for all six shells together, calculated using Eq. (3). Pair matching can reduce HPD due to integrated stress nonrepeatability by a factor of 5.

uniform film stress error and may be useful together to increase the allowable film stress tolerance. In addition, these results indicate that, unless the coating (and NISC) process has a much larger nonrepeatability than inaccuracy, improving accuracy is likely more valuable than improving repeatability.

There may also be additional reduction in HPD, or a narrowing of the error bars in Fig. 9, from pair matching if pairs are selected from a larger set of mirrors. We have not evaluated any impact that pair matching may have on alignment tolerances. Pair matching may also have a negative impact on the telescope assembly schedule, which would need to be considered.

4 Nonuniform Integrated Stress

Many stress-balancing approaches, such as depositing front- and backside coatings, require that the integrated coating stress is uniform enough on both sides to enable effective balancing. The NISC methods mentioned in Sec. 1 allow compensation of nonuniform stress, as well as addressing uniform stress inaccuracy and nonrepeatability. Understanding how nonuniform integrated stress affects PSF blurring is critical for any of these stress compensation methods.

For single-layer iridium films, the *in situ* measurements of iridium film stress made by Broadway et al. are invaluable for understanding how significant nonuniform integrated stress may arise due to small thickness variation alone. As an iridium film grows, the integrated stress is tensile at very low thickness, passes through zero, and then becomes compressive with a fairly uniform slope (dN_f/dh_f). They demonstrated that it is possible to achieve an extremely small integrated stress of -0.05 N/m if the deposition is stopped at the right moment (the deposition pressure, which can be changed, determines the zero-stress film thickness). However, the integrated stress changes as the deposited thickness changes, at a rate of -2.8 to -4 N/m/nm, depending on the deposition pressure.[6] This implies that a small variation in thickness across a mirror would result in varying integrated stress. For example, a $\pm1\%$ thickness variation (as measured by Mori et al.[9]) on a nominal 15 nm film would result in a variation in integrated stress of ±0.4 to ±0.6 N/m. In this section, we only consider a small thickness variation and assume
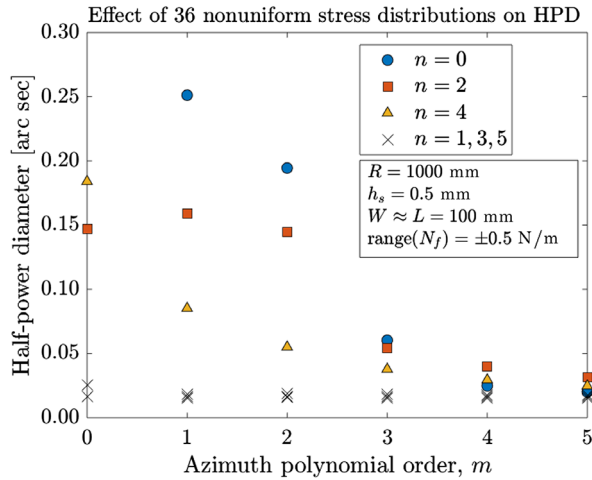
Fig. 10 HPD resulting from nonuniform film stress distributions, described by 2-D Legendre functions L_{mn}, with azimuthal order m and axial order n. Each stress distribution has peak values of ± 0.5 N/m. The distribution L_{00} is a uniform stress and is not shown here.

Fig. 11 Variation of HPD as a function of radius, for a few representative stress distributions $[N_f(\theta, z) = L_{mn}]$, each with peak values of ± 0.5 N/m. The stress distributions that most strongly affect HPD are usually monotonically increasing with radius, while L_{30} is representative of many stress distributions that have a smaller effect on HPD.

the stress is uniform. In reality, any stress variation would also contribute to integrated stress variation.

To illustrate the PSF blurring that can result from nonuniform integrated stress, we applied 36 different stress distributions to the FE model, with peak values of ± 0.5 N/m. We then calculated the HPD using the linearized ray tracing method. The stress distributions are described by two-dimensional (2-D) Legendre functions, $L_{mn}(\theta, z)$, which are the products of a Legendre polynomial (of order m) in the azimuthal direction and a Legendre polynomial (of order n) in the axial direction. For this work, we used up to fifth-order Legendre polynomials in each direction. For uniform stress, the HPD for $R = 1000$ mm is closest to the HPD for all shells together, so we show the HPD resulting from each of the stress distributions, for this radius, in Fig. 10. The deformation that results from a stress distribution that has an axial polynomial of odd order is asymmetric, so the primary and secondary mirror slopes largely cancel to produce a small HPD contribution. Figure 11 shows, for a few representative distributions, the variation of HPD with the shell radius.

We compared the linearized ray tracing method and full ray tracing for these 36 cases, and the RMS difference between the two calculations is 2%, within the standard deviation of HPD from full ray tracing. We also compared the linearized ray tracing method to the diffraction calculation of Raimondi and Spiga[28] (as described in Sec. 2.2 of this paper). For a shell radius of 1000 mm, we applied stress distributions described by each Legendre function for $0 \leq m \leq 5$ and $n = 0, 2, 4$ (which are the Legendre functions that have the most significant effect on HPD), with a magnitude that results in a 0.5 arc sec HPD according to the linearized ray trace method. We performed the diffraction calculation on eight axial traces of the mirror pair and calculated the HPD from the average of the eight PSFs. The aperture diffraction of 1 keV x-rays for this mirror pair is about 0.07 arc sec (see Fig. 3). For the 18 cases tested, the linearized ray tracing resulted in an HPD that was on average 1% larger than the diffraction calculation, and the mean difference was 10%. The discrepancy was larger for stress distributions with higher spatial-frequencies. For example, for $m = 5$ and $n = 0, 2, 4$, the linearized ray trace overestimated the
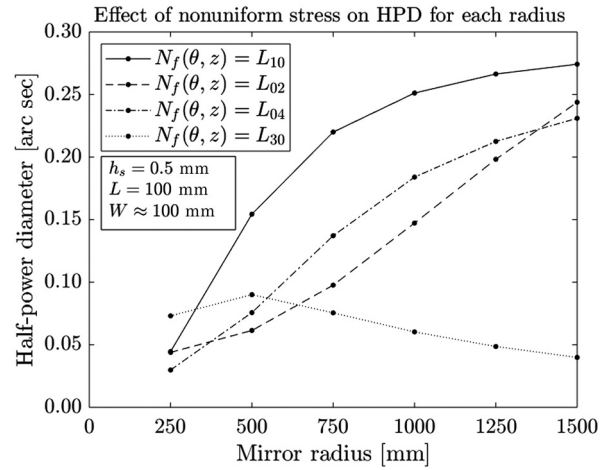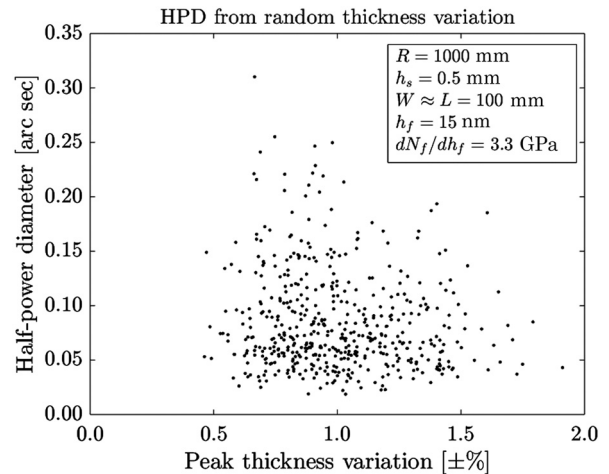

Fig. 12 The effect of small random thickness variation on HPD, for 500 random stress distributions on a mirror with radius of 1000 mm. The peak thickness variation is calculated from the integrated stress using Eq. (5). The mean HPD for these cases is 0.085 arc sec, with a standard deviation of 0.046 arc sec. The mean peak thickness variation is 1.0%, with a standard deviation of 0.3%.

HPD by 50%, 15%, and 17%, respectively. However, since the effects of higher-order stress distributions on HPD are generally smaller than low-order stress distributions, our estimate of HPD from a linear combination of stress distributions, discussed below, will not be significantly affected by this discrepancy. For smaller deformation, diffraction may have a more significant effect than shown here. As in Sec. 2.1, the PSFs of mirrors with smaller radii are dominated by aperture diffraction.

Generally, the integrated stress distribution on a mirror will be a linear combination of multiple Legendre functions, rather than a single Legendre function. Figure 12 shows the HPD that results from 500 randomly generated linear combinations of stress functions. For these cases, each Legendre function is assigned a normally distributed stress magnitude. Assuming that the stress distribution is only caused by film thickness variation, the peak film thickness variation, ε, is calculated from

$$\varepsilon = \frac{\pm \frac{1}{2}(\max N_f - \min N_f)}{(\mathrm{d}N_f/\mathrm{d}h_f)_{\mathrm{dep}}h_f}, \qquad (5)$$

where $(\mathrm{d}N_f/\mathrm{d}h_f)_{\mathrm{dep}}$ is the slope of the stress–thickness curve during deposition and is assumed to be -3.3 N/m/nm here ($N_f = \pm 0.5$ N/m and $h_f = 15$ nm corresponds to $\varepsilon \approx \pm 1\%$), which is consistent with the data from Ref. 24. It is clear from the figure that the HPD resulting from nonuniform integrated stress depends strongly on the particular distribution, but many of these distributions may be problematic for Lynx.

For these 500 cases, we found that scaling the HPD values from Fig. 10 and combining as a root sum-of-squares (RSS) does not produce a close estimate of the HPD calculated from the linearized ray tracing method. The mean difference between these two HPD calculations is 40%, and the RSS calculation is 30% too high, on average.

5 Postmounting Integrated Stress Change

Once Lynx is launched, any change to the mirrors could result in a broadening of the PSF. For example, a mirror may be thermally unbalanced, with iridium (or other films) on a silicon substrate. The mismatch in the coefficients of thermal expansion (CTE) between these two materials will cause a deformation that is dependent on temperature, even without temperature gradients. A similar effect would occur if the film stress relaxes over time. Identical films deposited on both sides of the mirror might reduce both the thermal and relaxation effects. In this section, we consider a mirror that experiences a uniform temperature change of $\pm 1^{\circ}\mathrm{C}$ since telescope assembly.

We discussed the FE model for a mounted mirror in Sec. 2.3. For a thin film of uniform thickness, the integrated stress N_f resulting from a temperature change ΔT can be calculated from the substrate and film properties as

$$N_f = \frac{E_f h_f}{1 - \nu_f}(\alpha_s - \alpha_f)\Delta T, \qquad (6)$$

where E_f and ν_f are the film elastic modulus and Poisson's ratio, h_f is the film thickness, and α_f and α_s are the film and substrate CTEs, respectively. As described in Sec. 2.3, the substrate elastic properties do not significantly affect the integrated stress, since the film is extremely thin compared to the substrate. If a thin coating is composed of multiple layers, the total integrated stress is simply the sum of the contributions from each layer. For relaxation, the quantity $(\alpha_s - \alpha_f)\Delta T$ can be replaced by the relaxation strain in the film.

For a 15 nm iridium film ($\alpha_f = 6.21$ ppm/K[38]) on a silicon substrate ($\alpha_s = 2.57$ ppm/K[39]), the integrated stress is 0.039 N/m-°C. Figure 13 shows the broadening of the PSF as a result of a $\pm 1^{\circ}\mathrm{C}$ temperature change. This data were calculated using the linearized ray tracing method.

The deformation, in this case, is quite small. For a 15-nm iridium film on a silicon substrate, the bulk temperature requirements for Lynx may not need to be much better than $\pm 1^{\circ}\mathrm{C}$ for this particular error term. However, for thicker multilayer films, or thick films on the mirror backside, these effects should be considered. The data in Fig. 13 may be scaled linearly with the integrated stress, so given an error allocation for allowable PSF blurring from stress relaxation or bulk temperature changes, the allowable relaxation or temperature can be easily calculated from these data.
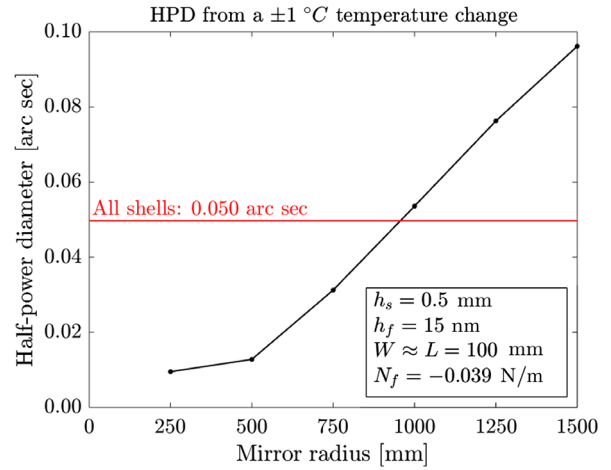

Fig. 13 HPD resulting from a $\pm 1^{\circ}\mathrm{C}$ temperature change of a silicon mirror with a 15 nm iridium film. The horizontal red line is the HPD estimate from all shells together, calculated using Eq. (3).

6 Conclusions

To ensure that Lynx is able to achieve its science objectives, the mirrors of the telescope must produce a PSF with a ~ 0.5 arc sec HPD, a challenging target. One important source of PSF blurring is the mirror deformation that results from a stressed reflective film, such as iridium or multilayers. It is well known that segmented mirrors are much more affected by film stress than full-shell mirrors. We have investigated the effects of film stress on the HPD of individual mirror shells composed of silicon mirror segments, as well as estimating the HPD from six shells together.

Integrated stress is inherent to sputtered films, but ideally would be uniformly zero on every mirror segment. We have reported the PSF blurring that occurs when the film stress is inaccurate, nonrepeatable, nonuniform, or varying after mounting. For film stress that is uniform and repeatable but inaccurate, we evaluated the benefit of compensating for the inaccuracy during mirror alignment. We found a 2.3× reduction in HPD, but this requires significant alignment changes even for a small integrated film stress. For film stress that is uniform and accurate but nonrepeatable, we evaluated the benefit of matching pairs of mirrors, and we found a 5× improvement. For nonuniform integrated stress, we found that even a $\pm 1\%$ film thickness nonuniformity could result in significant PSF blurring, but this depends strongly on the particular stress distribution. Finally, we found that a 15-nm iridium film on a silicon substrate produces a small amount of PSF blurring for a bulk temperature change of $\pm 1^{\circ}\mathrm{C}$, but this effect should be considered for other films, especially if thick films are used.

All of the results presented in this paper scale linearly with the magnitude of integrated stress (up to at least 2 N/m). In addition, in Sec. 2.3, we described numerous other ways in which these results may be accurately scaled. However, we found that increasing the mirror thickness reduces the HPD far less rapidly than for a flat plate, which limits how well film stress effects can be mitigated by thickening mirrors. We also found that the HPD resulting from a nonuniform stress distribution that is composed of many Legendre functions is not well approximated by an RSS of the HPD resulting from each individual Legendre function. The film stress accuracy, repeatability, and uniformity requirements for Lynx will likely be quite small, but they might be

achievable by using a combination of the many approaches under development within the x-ray astronomy community. For example, while the various film deposition strategies can produce excellent integrated stress accuracy, nonuniformity is a constant challenge. The various NISC methods can compensate for nonuniform film stress and can improve both accuracy and repeatability, but will likely be insufficient if the integrated film stress is not small to begin with. The key will be to find a set of methods that are mutually compatible, produce excellent x-ray reflectivity, and extremely small and uniform integrated stress.

Many of the errors considered in this paper could benefit from more in-depth analysis. It is worth considering the problems that could arise from either realigning mirrors or pair matching to compensate for inaccuracy or nonrepeatability, respectively. We did not consider how these approaches might affect alignment sensitivity, gravity release errors, cost, and schedule. Regarding film thickness nonuniformity, it would be valuable to measure actual film thickness distributions, since this strongly affects the calculated results.

Acknowledgments

References

1. J. A. Gaskin et al., "The Lynx X-ray Observatory: concept study overview and status," *Proc. SPIE* **10699**, 106990N (2018).
2. W. W. Zhang et al., "Astronomical x-ray optics using mono-crystalline silicon: high resolution, light weight, and low cost," *Proc. SPIE* **10699**, 106990O (2018).
3. C. T. DeRoo et al., "Deterministic figure correction of piezoelectrically adjustable slumped glass optics," *J. Astron. Telesc. Instrum. Syst.* **4**(1), 019004 (2018).
4. M. M. Civitani et al., "Thin fused silica shells for high-resolution and large collecting area x-ray telescopes (like Lynx/XRS)," *Proc. SPIE* **10399**, 103990W (2017).
5. R. E. Riveros et al., "Fabrication of lightweight silicon x-ray mirrors for high-resolution x-ray optics," *Proc. SPIE* **10699**, 106990P (2018).
6. D. M. Broadway et al., "Achieving zero stress in iridium, chromium, and nickel thin films," *Proc. SPIE* **9510**, 95100E (2015).
7. K.-W. Chan et al., "Reflective coating for lightweight x-ray optics," *Proc. SPIE* **8443**, 84433S (2012).
8. K.-W. Chan et al., "Coating thin mirror segments for lightweight x-ray optics," *Proc. SPIE* **8861**, 88610X (2013).
9. H. Mori et al., "Reflective coatings for the future x-ray mirror substrates," *Proc. SPIE* **10699**, 1069941 (2018).
10. D. D. M. Ferreira et al., "Performance and stability of mirror coatings for the ATHENA mission," *Proc. SPIE* **10699**, 106993K (2018).
11. D. M. Broadway et al., "In-situ stress measurement of single and multilayer thin-films used in x-ray astronomy optics applications," *Proc. SPIE* **10399**, 103991B (2017).
12. Y. Yao et al., "Design and fabrication of a supermirror with smooth and broad response for hard x-ray telescopes," *Appl. Opt.* **52**(27), 6824–6833 (2013).
13. F. Özel and A. A. Vikhlinin, "Lynx interim report" https://wwwastro .msfc.nasa.gov/lynx/docs/LynxInterimReport.pdf (10 April 2018).
14. P. J. Serlemitsos et al., "Multilayer option for conical foil x-ray mirrors," *Proc. SPIE* **3113**, 244–253 (1997).
15. L. M. Cohen and M. Foster, "XRS/Lynx: simulations regarding coating stress, segmented optics, and full shell optic comparative case," in *Presentation to the Lynx Optics Working Group* (2017).
16. G. Parodi, "Linx project mirror module proposal, MM configuration trade-off," in *Presentation to the Lynx Optics Working Group* (2018).
17. D. L. Windt, "Reduction of stress and roughness by reactive sputtering in W/B4C x-ray multilayer films," *Proc. SPIE* **6688**, 66880R (2007).
18. T. Döhring et al., "Development of low-stress Iridium coatings for astronomical x-ray mirrors," *Proc. SPIE* **9905**, 99056V.
19. A. Ames et al., "Using iridium films to compensate for piezo-electric materials processing stresses in adjustable x-ray optics," *Proc. SPIE* **9603**, 96031I (2015).
20. Y. Yao et al., "Thermal oxide patterning method for compensating coating stress in silicon x-ray telescope mirrors," *Proc. SPIE* **10699**, 1069942 (2018).
21. Y. Yao et al., "Thermal oxide patterning method for compensating coating stress in silicon substrates," *Opt. Express* **27**(2), 1010–1024 (2018).
22. B. D. Chalifoux et al., "Compensating film stress in silicon substrates for the Lynx x-ray telescope mission concept using ion implantation," *Proc. SPIE* **10699**, 1069959 (2018).
23. D. L. Windt and R. Conley, "Two-dimensional differential deposition for figure correction of thin-shell mirror substrates for x-ray astronomy," *Proc. SPIE* **9603**, 96031H (2015).
24. C. Atkins et al., "Differential deposition correction of segmented glass x-ray optics," *Proc. SPIE* **9603**, 96031G (2015).
25. Y. Yao et al., "Stress manipulated coating for fabricating lightweight x-ray telescope mirrors," *Opt. Express* **23**(22), 28605–28618 (2015).
26. X. Wang et al., "Deformation of rectangular thin glass plate coated with magnetostrictive material," *Smart Mater. Struct.* **25**(8), 85038 (2016).
27. H. E. Zuo et al., "Ultrafast laser micro-stressing for correction of thin fused silica optics for the Lynx X-Ray Telescope Mission," *Proc. SPIE* **10699**, 1069954 (2018).
28. L. Raimondi and D. Spiga, "Mirrors for x-ray telescopes: Fresnel diffraction-based computation of point spread functions from metrology," *Astron. Astrophys.* **573**, A22 (2015).
29. L. P. VanSpeybroeck and R. C. Chase, "Design parameters of paraboloid-hyperboloid telescopes for x-ray astronomy," *Appl. Opt.* **11**(2), 440–445 (1972).
30. R. C. Chase and L. P. VanSpeybroeck, "Wolter–Schwarzschild telescopes for x-ray astronomy," *Appl. Opt.* **12**(5), 1042–1044 (1973).
31. E. Gullikson, "Layered mirror reflectivity," http://henke.lbl.gov/ optical_constants/layer2.html (accessed 5 July 2018).
32. M. A. Hopcroft, W. D. Nix, and T. W. Kenny, "What is the Young's modulus of silicon?" *J. Microelectromech. Syst.* **19**(2), 229–238 (2010).
33. S. F. Pugh, "XCII. Relations between the elastic moduli and the plastic properties of polycrystalline pure metals," *Lond. Edinburgh, Dublin Philos. Mag. J. Sci.* **45**(367), 823–843 (1954).
34. B. D. Chalifoux, "Figure correction of thin plate and shell substrates using stress generated by ion implantation," PhD Thesis, Massachusetts Institute of Technology (2019).
35. K.-W. Chan et al., "Alignment and bonding of silicon mirrors for high-resolution astronomical x-ray optics," *Proc. SPIE* **10699**, 1069940 (2018).
36. S. Suresh and L. B. Freund, *Thin Film Materials: Stress, Defect Formation and Surface Evolution*, Cambridge University Press, Cambridge, United Kingdom (2009).
37. P. B. Reid et al., "A comparison of different alignment approaches for the segmented grazing incidence mirrors on Constellation-X," *Proc. SPIE* **7011**, 701111 (2008).
38. H. P. Singh, "Determination of thermal expansion of germanium, rhodium and iridium by x-rays," *Acta Cryst. A* **24**(4), 469–471 (1968).
39. H. Watanabe, N. Yamada, and M. Okaji, "Linear thermal expansion coefficient of silicon from 293 to 1000 K," *Int. J. Thermophys.* **25**(1), 221–236 (2004).

Biographies of the authors are not available.